RESEARCH ARTICLE

Synthesis of Nitrogen-doped $KTaTeO_6$ with Enhanced Visible Light Photocatalytic Degradation of Methylene Blue

Mannepalli Sudheera[1], Perala Venkataswamy[2], Gundeboina Ravi[2], Kadari Ramaswamy[2,3], Nalluri Chitti Babu[4], Muga Vithal[2,*]

[1]Department of Chemical Engineering, RVR & JC College of Engineering, Chowdavaram, Guntur 522 019, India
[2]Department of Chemistry, Osmania University, Hyderabad 500 007, India
[3]Centre for Materials for Electronics Technology (C-MET), Cherlapally, HCL (PO), Hyderabad 500 051, India
[4]Department of Chemical Engineering, Andhra University, Visakhapatnam 530 003, India

*Corresponding author: E-mail: mugavithal@gmail.com; Tel.: (+91) 40-27682337, Fax: (+91) 40-27090020

DOI: 10.5185/amlett.2021.041621

Anion doping is one of the efficient ways to tailor the bandgap of photocatalysts for the treatment of polluted water. The present work describes the improved photocatalytic activity of defect pyrochlore, $KTaTeO_6$ (KTTO), upon nitrogen doping, towards the degradation of methylene blue under visible light irradiation. The parent $KTaTeO_6$ was synthesized by solid-state method. The N-doped $KTaTeO_6$ (N-KTTO) was prepared by nitridation method using NH_3. Techniques such as the XRD, N_2 adsorption-desorption, FE-SEM/EDX/EDS elemental mapping, TEM-HRTEM, UV-Vis DRS, XPS, Raman, and PL were employed to characterize the physicochemical properties of photocatalysts. The N-doping in KTTO has resulted in enlarged surface area, narrowed the bandgap, and reduced the recombination of photogenerated electron-hole pairs, leading to enhanced photocatalytic activity compared to parent KTTO. The active species trapping experiments were conducted to elucidate the mechanism of photodegradation. The N-KTTO is chemically stable and can be used at least up to five cycles.

Introduction

Discharging an enormous quantity of organic dyes from textile, cosmetic, plastic, paper, printing, paints, and other dying industries into water has led to serious environmental concerns, especially to the water ecosystem [**1-4**]. Further, the residual organic dyes in water are responsible for various health hazards to humans and other living bodies that have also proven to be incurable [**5**]. Among the organic dyes, methylene blue (a thiazine (cationic) dye) was identified as a hazardous pollutant due to its mutagenic and carcinogenic nature [**6,7**]. It is known that MB dye causes increased heart rate, tissue narcosis, jaundice, vomiting, diarrhea, quadriplegia, nausea, and shock in humans [**8-10**]. So, there is a strong necessity for the treatment of effluents containing such dye from various industrial wastewaters. In this regard, semiconductor-mediated photocatalysis is currently emanated as an efficient technology for the degradation of organic pollutants present in the wastewater compared to traditional physicochemical methods [**11,12**]. The most attractive features of this process involve ambient conditions for reactions, the use of air as a source of oxygen for oxidation, eco-friendly nature, and an insignificant generation of secondary pollutants [**13-15**]. A large number of semiconductor materials including TiO_2 (a benchmark photocatalyst) have been synthesized and reported to be active for degradation of dyes [**16-18**]. However, a severe disadvantage of these oxides is their wide bandgap energies, which is too wide to absorb visible light [**19**]. Thus, searching potential photocatalysts that work under visible light irradiation is a challenge in the field of photocatalysis.

Quaternary oxides of type $ABB'O_6$ (A monovalent cation, B and B′ are penta & hexavalent cations) with defect pyrochlore structure have drawn the attention of researchers because of their technically important properties in addition to wide range of possible elemental combinations, highly interesting crystal structures, and bandgap tailoring feasibility (by cation/anion doping) [**20, 21**]. Ikeda *et. al.*, first reported the photocatalytic water splitting ability of a series of tungsten-containing oxides ($AMWO_6$; A = Rb, Cs; M = Nb, Ta) with defect pyrochlore structure under UV light irradiation [**22,23**]. Since then, different defect pyrochlores containing transition metals such as tantalum, niobium, tungsten, and titanium as promising photocatalysts have been studied for the decomposition of organic dyes and splitting of water for hydrogen production [**24-28**]. Tellurium containing defect pyrochlores has attracted much attention for photocatalysis and especially for dye degradation owing to their favorable properties, such as non-toxicity, chemical inertness, and high stability under light irradiation. Recently, Waehayee *et. al.*, synthesized the $KNbTeO_6$ and ion-exchanged with Ag^+, Cu^{2+}, and Sn^{2+} for photodegradation of methylene blue under visible light

irradiation [**29**]. A wide range of tellurium-based photocatalysts including $MSn_{0.5}Te_{0.5}O_6$ (M = K, Ag, $Cu_{0.5}$ and $Sn_{0.5}$), $KM_{0.33}Te_{1.67}O_6$ (M = Al, Cr, Fe), Ag^{+}/Sn^{+2} substituted $KTi_{0.5}Te_{1.5}O_6$ and $KSbTeO_6$ have been used in photocatalytic dye degradation studies [**30-33**]. Recently, we have studied the preparation, characterization, and photocatalytic activity towards the degradation of methyl violet and hydrogen evolution studies of $KTaTeO_6$ and Ag-doped $KTaTeO_6$ in the visible-light and solar light irradiation, respectively [**34**]. Further modulation of the intrinsic properties of $KTaTeO_6$ is strongly required to meet the rapidly increasing demand for practical applications in photocatalysis field.

In addition, doping with heteroatoms such as nitrogen/sulfur/fluorine into defect pyrochlore lattice has been proved to be an efficient method to improve the photocatalytic performance of defect pyrochlores. The doping of nitrogen is of special interest, because the ionic radii of nitrogen and oxygen are comparable, and the mixing of 2p levels of oxygen and nitrogen decreases the energy gap of the photocatalysts significantly [**35,36**]. It has been reported by Sun *et. al.,* that N-doping in $HTaWO_6$ can considerably reduce the bandgap of $HTaWO_6$ by elevating the valence band maximum [**37**]. Marschall *et. al.*, proposed that the substitutional co-doping of sulfur/nitrogen into the $CsTaWO_6$ lattice causes a significant shift of the absorption edge in the visible region because the S 2p/N 2p states contribute to the band-gap narrowing by mixing with the O 2p states [**38**]. Based on these reports, an attempt is made to incorporate nitrogen into $KTaTeO_6$ lattice with the expectation of improving the light absorption property of $KTaTeO_6$ in the visible region. In this investigation, we present the visible light driven photocatalytic properties of N-doped $KTaTeO_6$ against MB degradation and a comparison with parent $KTaTeO_6$.

Experimental

Materials

Analytical grade potassium carbonate (SDFCL, 99.99%), tantalum pentoxide (Sigma Aldrich, 99.99%), tellurium dioxide (Sigma Aldrich, 99.99%), and acetone (Sigma Aldrich, 99.8%) were purchased and used as received without any further purification. Milli-Q water was used for all the photocatalytic experiments.

Synthesis of $KTaTeO_6$ and N-doped $KTaTeO_6$

The parent $KTaTeO_6$ catalyst was synthesized by a conventional solid-state reaction as reported [**34**]. Briefly, K_2CO_3, Ta_2O_5, and TeO_2 were mixed with K:Ta:Te molar ratio of 0.5:0.5:1 and thoroughly ground in an agate mortar for 90 min in the presence of acetone (≈ 10 mL). Acetone, a low boiling point liquid, helps in mixing the reactants at molecular level and can easily be vaporized. The resultant finely crushed powder was loaded into an alumina crucible and successively heated in a muffle furnace at 300 °C for 5 h, 400 °C for 10 h, and at 600 °C for 16 h, with intermediate grinding after each heat treatment to ensure complete reaction. At the end of the final heat, the furnace was switched off. A brick red colored sample was obtained. The as-prepared $KTaTeO_6$ was subjected to the nitridation process to obtain N-doped $KTaTeO_6$. Parent $KTaTeO_6$ (0.5 g) was placed in an alumina crucible of 5 mL capacity and heated to 500 °C and kept at this temperature for 1.5 h under a flow of high purity ammonia gas at the rate of 100 mL min^{-1}. The gas flow continued until the furnace temperature reached to 50°C. A black colored sample, $KTaTeO_{6-x}N_y$, was obtained. The $KTaTeO_6$ and $KTaTeO_{6-x}N_y$ were labelled as KTTO and N-KTTO, respectively.

Characterizations

Powder X-ray diffraction (XRD) patterns were collected on a Rigaku miniplex diffractometer using Cu-Kα1 radiation (λ = 1.5406 Å) operated at 45 kV, 15 mA, and 25 °C. Fine powder samples were used for the XRD measurements and the intensity data were collected in the 2θ range of 10°−80° at 0.01°/min scanning speed and a counting time of 1s per step. The observed diffraction patterns were compared with the International Centre for Diffraction Data (ICDD) database. The structural refinement of the PXRD data was carried out by the Rietveld analysis method using Fullprof.2k program. The morphology of the samples was recorded by field-emission scanning electron microscopy (FE-SEM) using a Carl Zeiss model Ultra 55 electron microscope. Energy-dispersive X-ray spectroscopy (EDX) and mapping were used to determine the elemental composition and distribution of the representing elements on an OXFORD Inca detector interfaced at 5 kV. Transmission electron microscopy (TEM) and high-resolution transmission electron microscopy (HRTEM) were obtained using a JEOL JEM-2100F instrument equipped with a slow-scan CCD camera and an accelerating voltage of the electron beam of 200 kV. The TEM sample preparation was done by dispersing the powders in ethanol by ultra-sonication and then loaded onto perforated copper grids. The grids were air-dried before recording the micrographs. Nitrogen adsorption-desorption was used to detect the textural properties of the samples which was carried out on an ASAP 2020 M apparatus (Micromeritics Instrument Corporation) at 77K. The samples were degassed at 200 °C for 2h under vacuum to remove adsorbed impurities before measurement. The Brunauer-Emmett-Teller (BET) and Barret-Joyner-Halenda (BJH) methods were applied to calculate the specific surface area and pore size distribution, respectively. Diffuse reflectance UV-visible spectra (UV-Vis DRS) of powders were recorded at room temperature using JASCO V650 UV–Vis spectro-photometer in the range of 200–800 nm. The data obtained were converted to Kubelka–Munk (KM) functions. The pressed barium sulfate ($BaSO_4$) disc was used as the standard for these measurements. X-ray photoelectron spectroscopy (XPS) studies were performed using a K-α spectrometer (Thermo Scientific) with monochromatic Al-

Kα radiation (hϑ = 1486.7 eV) used as the radiation source at room temperature under ultra-high vacuum (10^{-8} Pa). The surface charging effect was calibrated by fixing the C 1s peak at a binding energy of 284.6 eV. The spectra were deconvoluted by using XPSPEAK software (Ver.4.1) after applying a Shirley background subtraction and Gaussian (80%)-Lorentzian (20%) decomposition parameters. Raman measurements were recorded under ambient conditions using a LabRam HR spectrometer (HORIBA Jobin Yvon, France) by keeping a sample in a microscopic glass slide with a 30 mW internal He-Ne (Helium-Neon) laser source with an excitation wavelength of 632.8 nm. Photoluminescence (PL) spectra were measured on a JASCO FP-8500 spectrofluorometer at room temperature with an excitation wavelength of 250 nm.

Photocatalytic activity studies

The photocatalytic activity of the prepared samples for the degradation of methylene blue (MB) was evaluated under visible light irradiation using a HEBER (Haber Scientific, model HVAR1234, India) annular type photo-reactor (Fig. S1, supporting information) equipped with a 300 W tungsten lamp as the light source (380 nm ≤ λ ≤ 840 nm). In a typical photocatalytic experiment, 50 mL of aqueous MB solution (initial concentration = $1*10^{-5}$ M) was stirred with 50 mg of the photocatalyst in a cylindrical-shaped glass tube reactor. The distance between the lamp and the tube containing photocatalyst and dye (methylene blue) is ~7–8 cm. Before light irradiation, the suspension was kept in the dark under stirring for 1 h to ensure an adsorption-desorption equilibrium between photocatalyst surface and MB dye molecules. At given intervals of 30 min, about 3 mL of the reaction solution was withdrawn from the photoreactor and subjected to centrifugation for 10 min to remove solid catalyst particles. Subsequently, the changes in the concentration of dye solution were monitored on a JASCO V650 UV-vis spectrophotometer by measuring the optical density at the wavelength of 664 nm, the λ_{max} of MB. A blank test was also carried out without a photocatalyst under similar conditions, to evaluate the efficiency of the photocatalyst.

To evaluate the presence of oxidant species during photocatalysis over the N-doped $KTaTeO_6$ system, the radical trapping experiments were performed. The benzoquinone (BQ), isopropyl alcohol (IPA), and ammonium oxalate (AO) were used as scavengers for superoxide ($^{\bullet}O^{2-}$) radical, hydroxyl ($^{\bullet}OH$) radical, and hole (h^{+}), respectively. For each scavenging experiment, a fixed concentration of scavenger i.e., 2mM was added into the reaction mixture. The method was similar to the above photocatalytic reaction. The formation of $^{\bullet}OH$ during photocatalysis under visible light irradiation was further substantiated by the measurement of fluorescence intensity of terephthalic acid. The fluorescence intensity of the reaction solution was measured on a Shimadzu RF-5301PC fluorescence spectrophotometer (λ_{exc} = 320 nm).

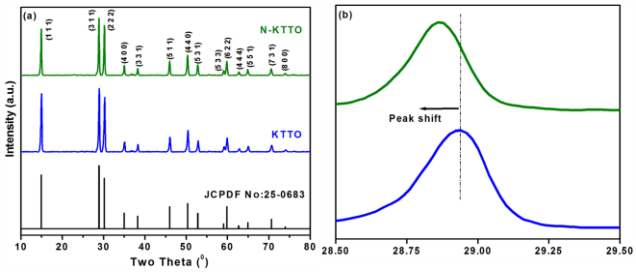

Fig. 1. (a) Powder XRD patterns (b) expanded XRD patterns showing shift in (311) plane of KTTO and N-KTTO.

Results and discussion

Powder XRD analysis

The phase identification of the KTTO and N-KTTO was investigated by the XRD analysis and the diffraction profiles are shown in **Fig. 1**. The XRD pattern of KTTO revealed a single-phase cubic pyrochlore with a space group Fd3m. The peak positions of KTTO well-matched with reference card JCPDS card No. 25-0683 [**34,39**]. The strong and sharp diffraction peaks with minimum noise (background) demonstrate high crystallinity of the samples. The XRD pattern of N-KTTO is similar to that of KTTO. No impurity phases were detected in the XRD patterns of both the samples indicating that the samples are phase-pure and crystallized in defect pyrochlore structure. It is noticed that when the diffraction pattern is plotted on an expanded scale, the Bragg plane (311) shows a clear shift of to the lower 2θ values compared to the parent KTTO [**Fig. 1(b)**]. This is due to the incorporation of the N into O sites of the $KTaTeO_6$ lattice and thus results in the formation of Ta/Te-N bonds. As the ionic radius of N^{3-} (1.46 Å) is slightly higher than that of O^{2-} (1.38 Å), the substitution of N^{3-} in O^{2-} sites is expected to enlarge the unit cell [**40**]. This result can also be confirmed from the lattice parameter (a) and unit cell volume (V) of both the samples obtained from the POWD analysis (**Table 1**) [**41**]. It can be seen that the lattice parameter and unit cell volume of N-KTTO is slightly higher than that of parent KTTO. Similar behaviour was reported in other nitrogen-doped defect pyrochlore oxides [**27,42**].

In addition, the diffraction peaks of N-KTTO were broadened and the peak intensity became lower, suggesting the small crystallite size for N-KTTO compared to that of parent KTTO. To substantiate this, the average crystallite size of parent KTTO and N-KTTO samples was calculated using the Scherrer equation for (311) peak. The calculated crystallite sizes were found to be 31.7 and 36.7nm for KTTO and N-KTTO, respectively.

Table 1. BET surface area (SA), pore size, pore volume, lattice parameter (LP) and lattice volume (LV) of KTTO and N-KTTO.

Sample	BET SA (m^2g^{-1})	Pore size (nm)	Pore volume (cm^3g^{-1})	LP (Å)	LV (Å^3)
KTTO	34	14.1	0.17	10.25	1076.89
N-KTTO	52	12.6	0.31	10.26	1078.81

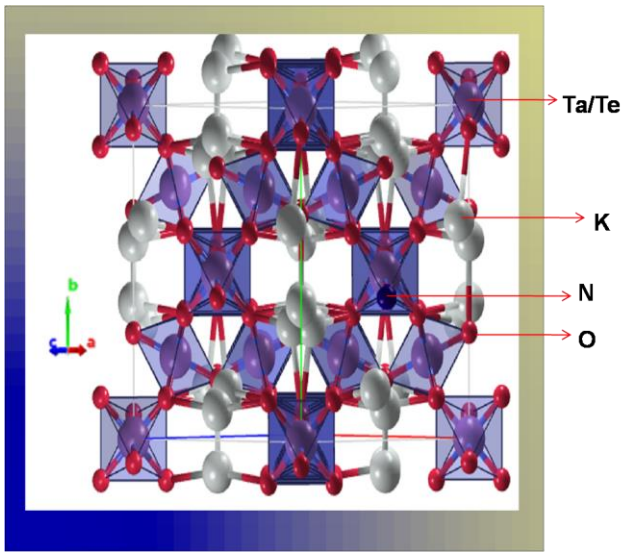

Fig. 2. Schematic crystal structure of N-KTTO.

Fig. 2 represents a fragment of the $KTaTeO_{6-x}N_y$ structure, which can be described as composed of a three-dimensional corner-sharing network of $(Ta/Te)O_6$ units forming the basic framework possessing tunnels with hexagonal cross-section down the *c*-axis. The K cations are situated in the interconnected channels coordinating to the six oxygen atoms of $(Ta/Te)O_6$ octahedron [**37,42,43**]. The nitrogen doping occurs due to the replacement of oxygen by nitrogen anions in the octahedron, which is indicated in **Fig. 2**. Based on the similarity of XRD pattern of N-KTTO with that of KTTO, the former is crystallized in cubic lattice with Fd3m.

Further structural characterization was carried out for N-KTTO by employing the Rietveld refinement program, FullProf.2k. The Rietveld refinement of the PXRD pattern of N-KTTO was carried out using the structural parameters of $KTaTeO_6$ in space group. A pseudo-Voigt function was chosen to generate the line shape of the diffraction peaks. The experimental and theoretical patterns deduced from Rietveld refinement are shown in Fig. S2 (supporting information). The Ta/Te cations and O/N ions are present in 16d (0, 0, 0) and 48f (0.326, 0.125, 0.125) Wyckoff positions, respectively. The Wyckoff position of potassium is 32e (0.347, 0.347, 0.347). The structural parameters obtained after refinement of N-KTTO is tabulated in Table S1 (supporting information). Further, the lattice parameter of N-KTTO is found to be a = 10.263 Å, which is slightly larger than that of KTTO (a = 10.251 Å) [**34**]. Therefore, these results confirm the incorporation of nitrogen into the crystal structure of KTTO.

FE-SEM/EDX/EDS elemental mapping and TEM-HRTEM studies

The surface morphology of KTTO and N-KTTO was obtained using FE-SEM and the results are shown in Fig. S3 (supporting information). As shown in this figure, parent KTTO is composed of hexagonal-shaped particles with more agglomeration (Fig. S3a), whereas, the N-KTTO particles have spherical-like morphology (Fig. S3b). Such spherical shape particles are well aligned to each other and distributed uniformly without much aggregation, which may give higher surface area and more exposed active sites. Furthermore, the EDX analysis was performed to determine chemical composition. The EDX spectrum of KTTO (Fig. S3c) shows the presence of K, Ta, Te, and O elements while the addition of N element peak was found in the EDX spectrum of N-KTTO (Fig. S3d), indicating that the nitrogen was doped into the KTTO lattice and the peak of energy at ~0.75 keV is attributed to nitrogen. The weight percentages of elements in KTTO and N-KTTO the samples obtained from EDX are given in Table S2 (supporting information). It is seen that the nitrogen content in N-KTTO is found to be 0.71 wt%. The EDS elemental mapping image indicates the uniform distribution of nitrogen atom throughout the surface of $KTaTeO_6$ thus confirming the incorporation of the nitrogen atom in KTTO lattice (Fig. S4; supporting information). Finally, the obtained EDX and elemental mapping results served as proof that the N-KTTO was free from impurities and the nitrogen was successfully incorporated into the KTTO lattice.

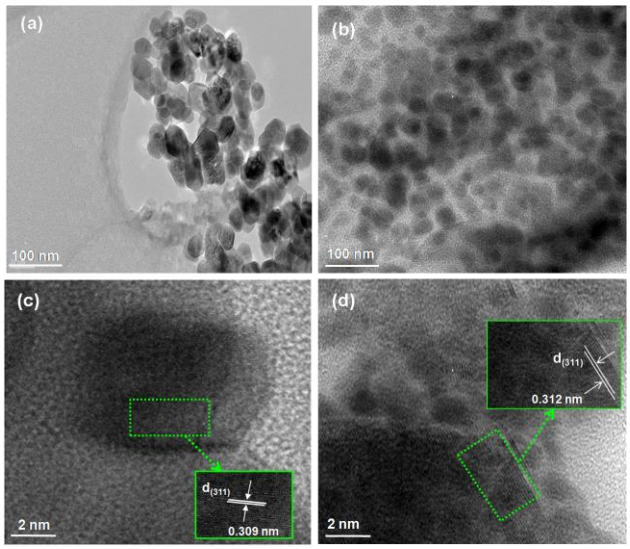

Fig. 3. TEM and HRTEM images of KTTO (a, c) and N-KTTO (b, d).

The TEM and HRTEM are beneficial for further understanding the morphology, crystallinity, and phase purity of the KTTO and N-KTTO catalysts. As shown in **Fig. 3(a)**, the TEM image of the KTTO shows agglomerated hexagonal-shaped particles; however, it could be observed that the N-KTTO was present in the form of spherical shape particles with uniform nature (**Fig. 3(b)**). The TEM results are consistent with the FE-SEM results discussed above. Moreover, clear lattice fringes observed in HRTEM images (**Fig. 3(c)** and **Fig. 3(d)**), confirm the good crystallinity of both samples. The lattice fringes with interplanar spacing corresponding to (311) plane in N-KTTO (0.312 nm) is found to be higher than that of KTTO (0.309 nm), which is also

consistent with the small shift observed in XRD. This result further confirms the phase purity and the incorporation of nitrogen into KTTO lattice.

Nitrogen adsorption-desorption

The surface area and pore structures are the crucial factors affecting the photocatalytic properties of the semiconducting oxides [**44**]. Therefore, the N_2 adsorption/desorption measurements were performed to investigate the surface area and pore structures of the KTTO and N-KTTO catalysts (Fig. S5; supporting information). It is observed that both samples exhibit the type-IV isotherm with different hysteresis loops as classified by the IUPAC, due to the capillary condensation steps at relative pressure (P/P_O) between 0.45 and 1.0, which is characteristic of the mesoporous structure of both samples [**45**]. The parent KTTO has the H1-type hysteresis loop, which is assigned to cylindrical pores. However, for the N-KTTO sample, the hysteresis loop changed to H3 type, which is generally reported for the slit-like pores formed by the aggregation of plate-like particles [**46**]. The existence of mesoporosity in these samples is further confirmed by the corresponding BJH pore size distribution shown in Fig. S5b. Unimodal pore size distribution was observed with an average pore size of 14.3 and 12.6 nm for KTTO and N-KTTO, respectively. The textural properties of KTTO and N-KTTO samples are listed in **Table 1**. The results show that the surface area of and pore volume of N-KTTO is higher than that of parent KTTO. The relatively larger surface area of N-KTTO would favour the adsorption of MB molecules on its surface and then benefit the subsequent degradation of MB molecules.

UV-Vis DRS

The optical absorption properties are pivotal in determining the photocatalytic activity of semiconducting oxides [**47**]. Therefore, to investigate the optical absorption characteristics of the synthesized photocatalysts, UV-Vis DRS profiles were recorded and the obtained results are shown in **Fig. 4**. It is observed that the KTTO and N-KTTO samples exhibit three intense peaks in the UV-region, which can be attributed to the oxygen-to-metal charge transfer transitions in the lattice [**34,48**]. Further, it is seen that both samples show strong absorption and steep absorption edges in the visible region. It implies that the samples are actively responsive to visible light. The absorption edge of parent KTTO was at about 562 nm, while the absorption edge of N-KTTO was at 715 nm, an obvious red shift of ~153 nm concerning KTTO. This result further confirmed the successful doping of N atoms into the $KTaTeO_6$ lattice thus led to the red-shift of the absorption edge. The extension of visible light absorption is also demonstrated by the colour change of the samples from bright yellow to black (**Fig. 4(a)** inset). The bandgap values of KTTO and N-KTTO are found to be 2.47 and 1.74 eV, based on the Kubelka-Munk function **(Fig. 4(b)** [**49**]. Further, the schematic band structure of KTTO and N-doped KTTO was shown in **Fig. 4(c)**. It is observed that the introduction of the nitrogen dopant leads to the up-shift of the valence band due to overlapping (mixing) of N 2p and O 2p, which narrowed the bandgap energy and extended the light-absorption range of parent KTTO. The obtained results are consistent with the previous reports on N-doping in metal oxides and other materials [**27,50,51**]. The smaller bandgap and increased absorption of light in the visible region by N-KTTO favour an increase in the production of electron-hole pairs and thereby higher photocatalytic activity.

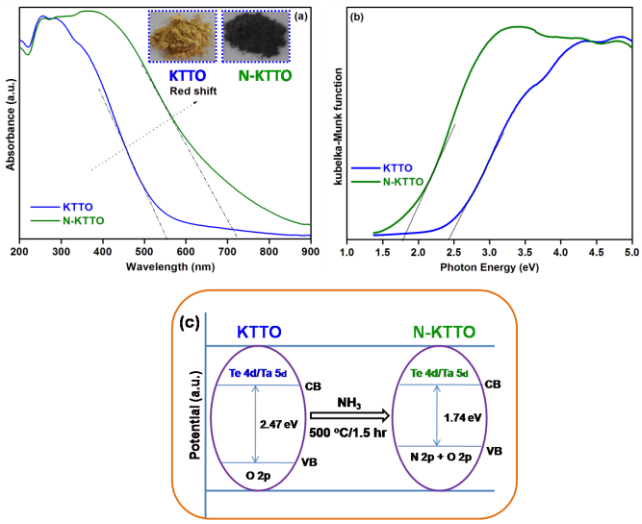

Fig. 4. (a) UV-Vis DRS spectra (inset shows the colour of respective samples) (b) Kubelka-Munk plot (c) Schematic band structures of KTTO and N-KTTO.

XPS

To further prove the presence of elements and their respective oxidation states in KTTO and N-KTTO catalysts, XPS analysis was also carried out. The binding energy of all elements present was calibrated using the C 1s peak at 284.6 eV. The survey scans of these catalysts are shown in Fig. S6 (supporting information). As depicted by the survey spectra in Figs. S6a and S6b, the full scan spectra show the well-recognized elements of K, Ta, Te, and O in KTTO, and K, Ta, Te, O, and N in N-KTTO. This is in accordance with the EDX results. Further, it is important to mention that no additional elements or impurities were observed. **Figs. 5(a)–5(e)** presents the XPS spectra of the K 2p, Ta 4d, Te 3d, O 1s, and N 1s, respectively. For the high-resolution XPS spectrum of K 2p in **Fig. 5(a)**, two peaks centered at 292.9 and 295.7 eV can be assigned to K $2p_{3/2}$ and K $2p_{5/2}$, respectively, and the binding energy difference between these two peaks of 2.8 eV corresponding to spin-orbit coupling, is consistent with the presence of K^{+1} species [**52**]. The Ta 4d spectrum shown in **Fig. 5(b)**, the observed peaks at 231.3 and 242.8 eV correspond to the Ta $4d_{7/2}$ and Ta $4d_{5/2}$, core-electron binding energies of Ta^{5+}, respectively. Likewise, **Fig. 5(c)** displays the spectrum of

Te 3d, the peaks at 576.5, and 587.1 eV are accredited to Te $3d_{5/2}$ and Te $3d_{3/2}$ peaks, respectively, which attribute to the existence of Te in a +6 oxidation state [**53**]. In addition, the high-resolution O 1s peak is deconvoluted to two sub-peaks in **Fig. 5(d)**, signifying two kinds of oxygen atoms in the samples, of which the low intense peak at 529.9 eV represents the crystal lattice oxygen (O1) bonded to the Ta/Te in the form of $(Ta/Te)O_6$ linkages, while the peak at 532.0 eV is assigned to surface hydroxyls or chemisorbed oxygen on the surface (O2) [**54**]. The higher amount of surface hydroxyl groups is beneficial to photocatalytic degradation since these species could react with photogenerated holes to generate hydroxyl radicals (•OH), which is believed to be the main active species in many photocatalytic processes [**55,56**]. Therefore, the relative amount of O2 in the samples can be calculated by the O2/O1+O2 ratio, and the obtained values are shown in **Fig. 5(d)**. It is seen that the O2 amount is higher in N-KTTO in comparison to parent KTTO. Hence, the higher O2 content is expected to accelerate the separation of photogenerated electron-hole pairs in N-KTTO and enhance its photocatalytic efficiency. The N 1s core-level XPS spectra of N-KTTO are shown in **Fig. 5(e)**, together with the parent KTTO sample as a reference. For both KTTO and N-KTTO samples, a strong peak positioned at 403.6 eV was observed which can be assigned to the Ta $4p_{3/2}$ [**57**]. After N-doping, an additional weak peak in the vicinity of Ta 4p centered at 395.5 eV was observed. According to the earlier XPS investigations on nitrogen-doped defect pyrochlores and TiO_2 catalysts, this peak can be attributed to β–N, namely anionic doping by substitution of lattice oxygen with nitrogen (substitutional N), resulting in a composition that can be described as $KTaTeO_{6-x}N_y$ [**37,58-60**]. This result indicates the formation of (Ta/Te)–N bonds in the O–(Ta/Te)–O network of the $KTaTeO_6$ catalyst. Therefore, it is believed that the presence of substitutional N species in the N-KTTO sample makes the main contribution to visible light absorption and visible light induced photocatalytic performance, as shown in the next section.

Raman spectra

To further investigate the effect of N-doping on KTTO, the as-synthesized samples are characterized by Raman spectra, and the corresponding results are shown in Fig. S7 (supporting information). The obtained Raman spectra of KTTO and N-KTTO are similar to each other, except small changes in intensity and positions of the bands. This result indicates that both KTTO and N-KTTO are crystallized in the same lattice, which is in good agreement with our XRD results. As shown in Fig. S7, a weak and broad band in the region of 250-306 cm^{-1} with maxima at 280 cm^{-1} and a shoulder peak at 460 cm^{-1} correspond to the O–Ta–O bending vibrations [**42,61**]. The prominent sharp and intense peak near 510 cm^{-1} is related to the A_{1g} symmetric stretching mode of $(Ta/Te)O_6$ octahedra [**33,62**]. The broad band in the high wavenumber region centered at 668 cm^{-1} can be assigned to the main Ta/Te–O stretching mode. After the N-doping, all the characteristic Raman bands shifted to higher wavenumber, in a range of 5–8 cm^{-1} depending on the vibrational mode. A similar result was also reported in the nitrogen-doped TiO_2 and other related photocatalysts [**63, 64**]. The Raman results demonstrated the formation of Ta/Te–O and Ta/Te-N bonds, which further confirmed the successful doping of N into $KTaTeO_6$ lattice.

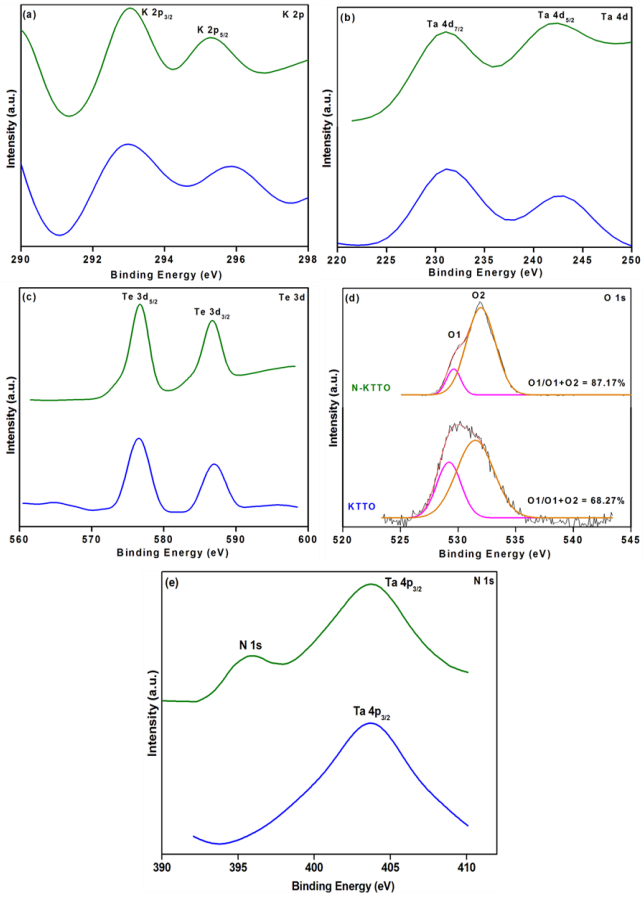

Fig. 5. XPS spectra of KTTO and N-KTTO: (a) K 2p (b) Ta 4d (c) Te 3d (d) O 1s and (e) N 1s.

PL spectroscopy

PL spectroscopy is an important characterizing technique to understand the recombination rate of the photoinduced electron-hole pairs in photocatalysts. It is generally well-known that the lower the intensity of PL peak means to lower the recombination rate of electron-hole and hence the higher photocatalytic activity [**65**]. Figure S8 (supporting information) depicts the room temperature PL emission spectra of KTTO and N-KTTO samples at an excitation wavelength of 250 nm. The observed PL emission peaks are due to the recombination of photogenerated electrons and holes. As seen in this figure, both samples are exhibiting main peaks at identical positions, but with different intensities. The lower PL emission peak intensity of N-KTTO suggests the recombination rate of electron-hole pairs is effectively prevented compared to parent KTTO. This phenomenon

might be attributed to the formation of intrinsic defects, such as oxygen vacancies, generated by the nitrogen doping [**10,66**]. Therefore, the lower PL emission peak of N-KTTO confirms its high efficiency in the separation of the electron-hole pairs, and hence higher photocatalytic activity is expected.

Photocatalytic activity studies

Based on the UV-Vis DRS results, both KTTO and N-KTTO have excellent optical absorption properties. Because of this, the photocatalytic activity of the parent KTTO and N-doped KTTO catalysts was assessed by measuring the degradation of the model organic dye, MB, under the visible light irradiation at room temperature. **Figs. 6(a)** and **6(b)** show the UV-vis spectral changes of MB aqueous solution as a function of irradiation time in the presence of KTTO and N-KTTO samples, respectively. As seen from the observed UV-vis spectra, the characteristic absorption peak intensity of MB dye (λ = 664 nm) decreases gradually with the increasing irradiation time for both catalysts. The photocatalytic degradation behaviour of MB with irradiation time on KTTO and N-KTTO is shown in **Fig. 6(c)**. A blank experiment without a catalyst for MB degradation under similar conditions was also carried out for comparison. It can be seen that the photocatalytic activity of MB without catalyst exhibit 22% degradation after 180 min, which accounts for the photosensitized capability of MB molecules (self-photolysis). The degradation efficiency of MB on KTTO was 82% within 180 min under visible light irradiation. After being doped with nitrogen, the degradation efficiency reached to 92%, revealing that the photocatalytic performance was distinctly enhanced. Previous research studies have manifested that photocatalytic activity depends on many properties of the catalyst, including the bandgap energy, the surface structure, separation of photoinduced electron-hole pairs, extent of crystallinity, the surface adsorbed hydroxyl/ water species and nature of pollutant [**29,67,68**]. In the present work, the observed higher photocatalytic performance of the N-KTTO sample could be attributed to the several beneficial effects produced by the doping of N into the lattice of KTTO. The improved photocatalytic activity of N-KTTO can be first understood by its lower bandgap energy, which facilitates an increase in the absorption efficiency of the visible light. According to the previous studies, the substitution of oxygen by nitrogen decreases the bandgap energy of parent oxides by shifting the valence band upward, which is corroborated with the UV–Vis DRS results [**50,59,69,70**]. It is known that catalysts with lower bandgap energies can harvest more photons to excite the electron from the valance band to the conduction band, which could increase the reaction rate by generating a large number of electron-hole pairs by absorption of visible light and results in the higher photocatalytic efficiencies. The lower bandgap energy, surface-adsorbed oxygen (substantiated from XPS), and lower recombination rate of electron-hole pairs due to oxygen vacancies (supported by PL analysis) are responsible for higher photocatalytic degradation of MB by N-KTTO. Moreover, the N-KTTO has a much larger BET surface area and smaller mesopores, which can provide abundant active sites to accelerating the adsorption and diffusion of MB dye molecules and then the MB degradation reaction can easily proceed at the surface. The kinetic data for the degradation of MB in the presence of KTTO and N-KTTO under the visible light irradiation is presented in **Fig. 6(d)**. It was found that the tendency of the curve is well concurrent with an apparent pseudo-first-order reaction model: $\ln (C/C_0) = k_{app}t$, where C_0 and C indicate the initial and final concentration of MB, respectively, t is the reaction time, and k_{app} signify the apparent rate constant [**71**]. The k_{app} value is measured from the slope of the linear line. In our experiment, the value of K_{app} for KTTO and N-KTTO is found to be 0.0099 and 0.0145 min^{-1}, respectively. The results show that the N-KTTO exhibits higher degradation efficiency of MB than that of KTTO. All the above results suggest that the N-KTTO exhibits superior photocatalytic activity than parent KTTO under visible light irradiation.

To know the role of photogenerated active species in MB degradation by as-synthesized N-KTTO under visible light irradiation, trapping experiments were performed by adding different scavengers like BQ, AO, and IPA for quenching $^{\bullet}O^{2-}$, h^+, and $^{\bullet}OH$, respectively [**65**]. The degradation efficiency of MB in the presence of N-KTTO and scavengers are shown in Fig. S9a (supporting information). As shown in this figure, it is evident that the photocatalytic degradation of MB by N-KTTO was decreased significantly by the addition of IPA, suggesting that the $^{\bullet}OH$ radicals could be the major active species in the degradation reaction. On the other side, it was also observed that $^{\bullet}O^{2-}$ and h^+ have a partial influence on dye degradation. Besides, the generation of $^{\bullet}OH$ radicals on the surface of N-KTTO was further probed by fluorescence technique using terephthalic acid (TA) as a probe molecule. It has been earlier reported that the non-fluorescent TA molecule reacts with $^{\bullet}OH$ to give a fluorescent product i.e., 2-hydroxyterephthalic acid (TAOH), which emits a unique fluorescence signal at a 425 nm [**72,73**]. Figure S9b (supporting information) reports the fluorescence spectra of the 2-TAOH obtained for N-KTTO with an excitation wavelength of 320 nm. As expected, the fluorescence intensity at 425 nm gradually increased with an increase in illumination time, indicating the generation of numerous $^{\bullet}OH$ in N-KTTO, which is consistent with the radical trapping experiment shown in Fig. S9a.

It is well established that the chemical stability and reusability of the photocatalyst is an important parameter concerning its practical applications [**12,74**]. Recycling experiments using N-KTTO were performed under identical conditions and in sequence for five cycles. At the end of each cycle, the used catalyst was recovered by centrifugation, washed several times with ethanol and distilled water, and used in the next cycle. Figure S9c

(supporting information) shows a plot of MB degradation efficiency vs. a number of cycles. From Fig. S9c, it can be observed that there is no significant decrease in the photocatalytic activity of N-KTTO. Even after five cycles, the degradation efficiencies of MB dye was around 86%, which demonstrated that N-KTTO is an efficient and stable photocatalyst. In order to prove the stability of the N-KTTO catalyst, the XRD result of used and fresh catalysts was compared, as shown in Fig. S9d. As seen, all of the diffraction peaks of the used catalyst are consistent with that of fresh catalyst, which proves the high stability of the N-KTTO during the degradation of MB.

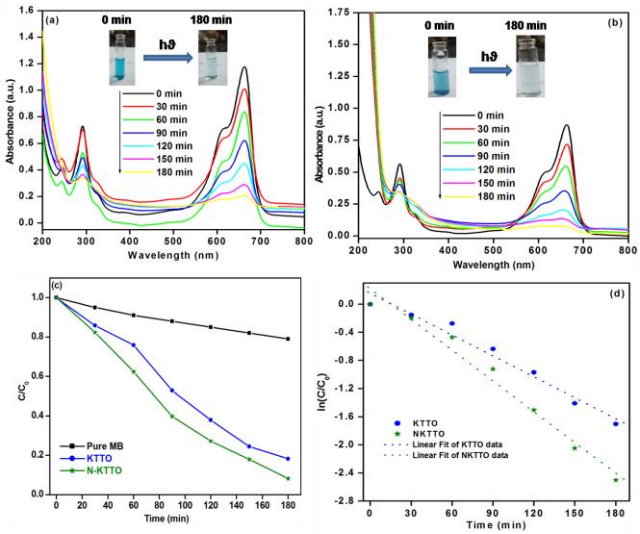

Fig. 6. (a) and (b) The UV-vis absorption spectra of MB solution as a function of irradiation time (the inserted photographs illustrate the color change) (c) Photocatalytic degradation rate of MB and (d) Pseudo-first-order kinetics fitted curves over KTTO and N-KTTO.

Mechanism of photoactivity of MB over N-KTTO

The possible mechanism for visible light induced photocatalytic degradation of MB over N-KTTO is schematically illustrated in Scheme 1. The mechanism can be explained by the following equations. Under visible light irradiation, initially, the electrons from the valence band of N-KTTO are excited to the conduction band leaving holes in the valence band (Eq. 1). The photogenerated electrons are reacting with adsorbed aqueous O_2 molecules, to form $^{\bullet}O^{2-}$ (Eq. 2). At the same time, due to the existence of oxygen vacancies, the O_2 can be converted into $^{\bullet}O^{2-}$ more easily on the surface [**75**]. Some of the $^{\bullet}O^{2-}$ further reacted with H_2O molecules that lead to the formation of H_2O_2 and finally reduced to the $^{\bullet}OH$, an active oxygen species (Eqs. 3-5) [**76-78**]. Likewise, the photogenerated h^+ species oxidize the hydroxyl ions to produce hydroxyl radicals (Eq. 6). The $^{\bullet}OH$ radicals formed in equations (5) and (6) are the prompts of photocatalytic reaction, which promotes the degradation of MB molecules. From the findings of this work, we believe that the N-doped $KTaTeO_6$ is considered to be an efficient and more active photocatalyst for decomposing the organic dyes from wastewaters with the visible light irradiation.

$$N-KTTO \rightarrow N-KTTO_{CB}(e^-)+N-KTTO_{VB}(h^+) \quad (1)$$

$$N-KTTO_{CB}(e^-)+O_2 \rightarrow \dot{O}_2^- \quad (2)$$

$$\dot{O}_2^- + H_2O \rightarrow \dot{H}O_2 + OH^- \quad (3)$$

$$2\dot{H}O_2 \rightarrow H_2O_2 + O_2 \quad (4)$$

$$H_2O_2 + \dot{O}_2^- \rightarrow \dot{O}H + OH^- + O_2 \quad (5)$$

$$N-KTTO_{VB}(h^+) + OH^- \rightarrow \dot{O}H \quad (6)$$

$$\dot{O}H + MB\ molecules \rightarrow CO_2 + H_2O \quad (7)$$

Conclusion

In conclusion, a phase pure N-doped $KTaTeO_6$ photocatalyst with defect pyrochlore structure has been successfully synthesized by nitridation of $KTaTeO_6$ under ammonia atmosphere at 500 °C. The characterization results showed that the structure was retained but the bandgap energy and photocatalytic properties were changed significantly by nitrogen doping. XRD results illustrated a slight shift of the (311) diffraction peak towards lower 2θ which can be due to the doping of the nitrogen. EDX and EDS mapping results confirmed the existence of nitrogen atoms in N-doped KTTO. Based on the weight ratio of elements, the nitrogen content in the N-KTTO sample was found to be 0.71 wt%. The observation of Ta/Te-O and Ta/Te-N bands in the XPS and Raman spectra indicate that some of the oxygen atoms in $KTaTeO_6$ are replaced by nitrogen (substitutable doping) and resulted in the formation of $KTaTO_{6-x}N_y$ catalyst. UV-Vis DRS results showed that the bandgap energy was considerably decreased from 2.47 to 1.74 eV, due to the up-shift of the valence band maximum caused by the hybridization between N 2p and O 2p states upon N-doping. The recombination of the photogenerated electron-hole pairs was efficiently reduced in N-KTTO, as evidenced by the PL results. In addition, it was demonstrated that N-KTTO exhibited higher surface area and surface adsorbed oxygen species, which were proved by N_2 adsorption/desorption and XPS results. As a result, the N-KTTO exhibited higher photocatalytic activity towards the degradation of MB under visible light irradiation in comparison to that of KTTO. Active species trapping studies proved that the photogenerated hydroxyl radicals played a major role in the photodegradation of MB. The reusability study has shown that the N-KTTO can be effectively recycled for five repetitive cycles and maintain a higher photocatalytic activity (>86%). This novel work will provide remarkable opportunities for the development of tellurium-based defect pyrochlore photocatalysts which can help in solving the environmental problems.

Acknowledgements

MS gratefully acknowledges the funding agency, University Grant Commission (UGC), India, for providing financial support, in the form of SERO/UGC. MV and PV would like to acknowledge the Department of Science and Technology-Science and Engineering Research Board (DST-SERB) of India for financially supporting this research under the Extramural Research (renamed as Core Research Grant) [File No: EMR/2016/001533]. MV thanks to UGC, New Delhi, India, for the award of BSR Faculty Fellowship [F.18–1/2011(BSR)].

Author's contribution

Sudheera: Synthesized the materials, performed the experiments, and prepared the first draft; **Venkataswamy:** Conceived the plan, performed the experiments, data analysis, and took the lead in writing the manuscript; **Ravi:** performed the Rietveld analysis; **Ramaswamy:** Performed and interpreted the FESEM/EDX analysis; **Chitti Babu:** Formal analysis, review & editing the manuscript. **Vithal:** Interpreted the results, supervision, project administration, resources, funding acquisition, discussed and finalized the manuscript with the co-authors.

Supporting information

Detailed information about the block diagram of the photocatalytic experimental set-up, structural parameters and diffraction pattern obtained after Rietveld refinement, wt% of elements from EDX, FE-SEM/EDX images, EDS elemental mapping images, nitrogen adsorption/desorption profiles, XPS survey spectra, Raman spectra, PL emission spectra, active species trapping experiment, Fluorescence spectra using terepthalic acid, recycling activity tests and the recovered catalysts XRD were given in the supplementary data.

Conflicts of interest

The authors declare that they have no conflict of interest that could have appeared to influence the work reported in this paper.

Keywords

Defect Pyrochlore, $KTaTeO_6$, N-doping, Bandgap energy, visible light absorption, $^{\bullet}OH$ radicals

Received: 8 August 2020
Revised: 7 September 2020
Accepted: 22 September 2020

References

1. Pan, D.; Ge, S.; Zhao, J.; Tian, J.; Shao, Q.; Guo, L.; Mai, X.; Wu, T.; Murugadoss, V.; Liu, H.; Ding, T.; Angaiah, S.; Guo, Z.; *Ind. Eng. Chem. Res.*, **2018**, *58*, 836.
2. Kuriakos, S.; Satpati, B.; Mohapatra, S.; *Adv. Mater. Lett.*, **2015**, *6*, 217.
3. Khatri, A.; Rana, P.S.; *Phys. B. Condens. Matter*, **2020**, *579*, 411905.
4. Li, D.; Liu, Y.; Liu, H.; Li, Z.; Lu, L.; Liang, J.; Huang, Z.; Li, W.; *Res. Chem. Intermed.*, **2020**, *46*, 1065.
5. Venkataswamy, P.; Sudheera, M.; Vaishnavi, K.; Ramaswamy, K.; Ravi, G.; Vithal, M.; *J. Electron. Mater.*, **2020**, *49*, 2358.
6. Bapat, P.; Nandy, S.K.; Wangikar, P.; Venkatesh, K.V.; *J. Microbiol. Methods*, **2006**, *65*, 107.
7. Malghe, Y. S.; Lavand, A. B.; *Adv. Mater. Lett.*, **2016**, *7*, 239.
8. Chowdhury, S.; Saha, P. D.; *Appl. Water Sci.*, **2012**, *2*, 209.
9. Mohapatra, P.; Parida, K.M.; *J. Molec. Catal. A Chem.*, **2006**, *258*, 118.
10. Rao, M.P.; Nandhini, V.P.; Wu, J.J.; Syed, A.; Ameen, F.; Anandan, S.; *J. Solid State Chem.*, **2018**, *258*, 647.
11. Venkataswamy, P.; Manasa, S.; Ravi, G.; Radha, V.; Vithal, M.; *Catal. Lett.*, **2019**, *149*, 2332.
12. Kumar, V.N.; Reddy, J.R.; Ravi, G.; Ravinder, G.; Venkataswamy, P.; Vithal, M.; *Chemistry Select*, **2016**, *1*, 2783.
13. Alosfur, F.K.M.; Ridha, N.J.; Jumali, M.H.H.; Radiman, S.; *Nanotechnology*, **2018**, *29*, 145707.
14. Wu, C.H.; Chern, J.M.; *Ind. Eng. Chem. Res.*, **2006**, *45*, 6450.
15. Kumar, V. N.; Ravi, G.; Reddy, J. R.; Suresh, P.; Muniratnam, N. R.; Prasad, G.; Vithal, M.; *J. Am. Ceram. Soc.*, **2014**, *97*, 1829.
16. Mzoughi, M.; Anku, W. W.; Oppong, S. O. B.; Shukla, S. K.; Agorku, E. S.; Govender, P. P.; *Adv. Mater. Lett.*, **2016**, *7*, 946.
17. Singh, J.; Sahu, K.; Kuriakose, S.; Tripathi, N.; Avasthi, D. K.; Mohapatra, S.; *Adv. Mater. Lett.*, **2017**, *8*, 107.
18. Singh, M.; Jampaiah, D.; Kandjani, A.E.; Sabri, Y.M.; Gaspera, E. D.; Reineck, P.; Judd, M.; Langley, J.; Cox, N.; van Emdben, J.; Mayes, E.; Gibson, B.C.; Bhargava, S. K.; Ramanathan, R.; Bansal, V.; *Nanoscale*, **2018**, *10*, 6039.
19. Shang, X.; Zhang, M.; Wang, X.; Yang, Y.; *J. Exp. Nanosci.*, **2014**, *9*, 749.
20. Ravinder, G.; Reddy, J.R.; Sudhakar, Reddy Ch.; Sreenu, K.; Ravi, G.; Vithal, M.; *Adv. Mater. Lett.*, **2016**, *7*, 536.
21. Martos, M.; Julian-Lopez, B.; Cordoncillo, E.; Escribano, P.; *J. Phys. Chem. B.*, **2008**, *112*, 2319.
22. Ikeda, S.; Itani, T.; Nango, K.; Matsumura, M.; *Catal. Lett.*, **2004**, *98*, 229.
23. Weiss, M.; Wirth, B.; Marschall, R.; *Inorg. Chem.*, **2020**, *59*, 8387.
24. Zhang, G.; Jiang, W.; Yu, S.; *Mater. Res. Bull.*, **2010**, *45*, 1741.
25. Liang, S.; Zhu, S.; Zhu, J.; Chen, Y.; Zhang, Y.; Wu, L.; *Phys. Chem. Chem. Phys.*, **2012**, *14*, 1212.
26. Schwertmann, L.; Wark, M.; Marschall, R.; *RSC Adv.*, **2013**, *3*, 18908.
27. Reddy, J. R.; Ravinder, G.; Kumar, V. N.; Shrujana, P.; Radha, V.; Vithal, M.; *J. Alloys Compd.*, **2015**, *618*, 815.
28. Uma, S.; Singh, J.; Thakral, V.; *Inorg. Chem.*, **2009**, *48*, 11624.
29. Waehayee, A.; Watthaisong, P.; Wannapaiboon, S.; Chanlek, N.; Nakajima, H.; Wittayakun, J.; Suthirakun, S.; Siritanon, T.; *Catal. Sci. Technol.*, **2020**, *10*, 978.
30. Ravinder, G.; Ravi, G.; Ramaswamy, K.; Sreenu, K.; Sudhakar, Reddy Ch.; Malathi, M.; Radha, V.; Vithal, M.; *Indian J. Chem.*, **2016**, *55A*, 1174.
31. Ravinder, G.; Ravi, G., Suresh, P.; Rao, K. N.; Vithal, M.; *Mater. Sci. Eng. B*, **2015**, *198*, 1.
32. Ravinder, G.; Ravi, G.; Reddy, J. R.; Kumar, V. N.; Sreenu, K.; Vithal, M.; *Photochem. Photobiol.*, **2016**, *92*, 223.
33. Ravinder, G.; Shrujana, P.; Kumar, V. N.; Ravi, G.; Rao, K. N.; Vithal, M.; *Chem. Pap.*, **2015**, *69*, 269.
34. Venkataswamy, P.; Sudhakar, Reddy Ch.; Ravi, G.; Sadanandam, G.; Kumar, V.N.; Vithal, M.; *Electron. Mater. Lett.*, **2018**, *14*, 446.
35. Tang, C.; Chen, C.; Zhang, H.; Zhang, J.; Li, Z.; *Phys. B Condens. Matter*, **2020**, *583*, 412029 (1–7).
36. Selvaraj, A.; Sivakumar, S.; Ramasamy, A. K.; Balasubramanian, V.; *Res. Chem. Intermed.*, **2013**, *39*, 2287.
37. Sun, C.; Mukherji, A.; Liu, G.; Wang, L.; Smith, S.C.; *Chem. Phys. Lett.*, **2011**, *501*, 427.
38. Marschall, R.; Mukherji, A.; Tanksale, A.; Sun, C.; Smith, S.C.; Wang, L.; Lu, G.Q.; *J. Mater. Chem.*, **2011**, *21*, 8871.
39. Darriet, B.; Rat, M.; Galyet, J.; Hagenmuller, P.; *Mater. Res. Bull.*, **1971**, *6*, 1305.
40. Shannon, R.D.; *Acta. Cryst. A*, **1976**, *32*, 751.
41. Wu, E.; *J. Appl. Cryst.*, **1989**, *22*, 506.
42. Mukherji, A.; Marschall, R.; Tanksale, A.; Sun, C.; Smith, S. C.; Lu, G.Q.; Wang, L.; *Adv. Funct. Mater.*, **2011**, *21*, 126.
43. Alonso, J.A.; Mayer, S.; Falcón, H.; Turrillas, X.; Fernández-Díaz, M. T.; *Crystals*, **2017**, *7*, 24.
44. Mohammad, A.; Khan, M.E.; Cho, M.H.; *J. Alloys Compd.*, **2020**, *816*, 152522.
45. Xue, C.; Wang, T.; Yang, G.; Yang, B.; Ding, S.; *J. Mater. Chem. A*, **2014**, *2*, 7674.
46. Zhou, Y.; Hu, W.; Yu, J.; Jaio, F.; *React. Kinet. Mech. Catal.*, **2015**, *581*, 115.
47. Hardcastle, F. D.; Wachs, I.E.; David, H.E.; Jefferson, A.; *J. Solid State Chem.*, **1991**, *90*, 194.
48. López, Nieto J.M.; Botella, P.; Solsona, B.; Oliver, J.M.; *Catal. Today*, **2003**, *81*, 87.
49. Sreenu, K.; Venkataswamy, P.; Ravi, G.; Sudhakar, Reddy Ch.; Reddy, B.J.; Vithal, M.; *Z. Anorg. Allg. Chem.*, **2019**, *645*, 529.
50. Suresh, P.; Ravinder, G.; Ravi, G.; Radha, V.; Vithal, M.; *Acta Metall. Sin. (Engl. Lett.)*, **2015**, *28*, 216.
51. Ni, M.; Leung, M.K.H.; Leung, D.Y.C.; Sumathy, K.; *Renew. Sustain. Energy Rev.*, **2007**, *11*, 401.
52. Li, S.; Kang, E. T.; Neoh, K.G.; Ma, Z.H.; Tan, K.L.; Huang, W.; *Appl. Surf. Sci.*, **2001**, *181*, 201.
53. Dubey, M.; Kumar, A.; Murugavel, S.; Prakash, G. V.; Jose, D. A.; Mariappan, C.R.; *Ceram. Int.*, **2020**, *46*, 663.
54. Zhua, J.; Chen, F.; Zhang, J.; Chen, H.; Anpo, M.; *J. Photochem. Photobiol. A*, **2006**, *180*, 196.
55. Bingham, S.; Daoud, W. A.; *J. Mater. Chem.*, **2011**, *21*, 2041.
56. Thirupathi, B.; Reddy, I.S.N.; Suidan, M.; Smirniotis, P. G.; *Chem. Eng. J.*, **2018**, *339*, 249.
57. Mukherji, A.; Sun, C.; Smith, S.C.; Lu, G.Q.; Wang, L.; *J. Phys. Chem. C*, **2011**, *115*, 15674.
58. Hoang, S.; Guo, S.; Hahn, N.T.; Bard, A.J.; Mullins, C. B.; *Nano Lett.*, **2012**, *12*, 26.

59. Wang, T.; Yan, X.; Zhao, S.; Lin, B.; Xue, C.; Yang, G.; Ding, S.; Yang, B.; Ma, C.; Yang, G.; Yang, G.; *J. Mater. Chem. A*, **2014**, *2*, 15611.
60. Xu, J.; Liu, Q.; Lin, S.; Cao, W.; *Res. Chem. Intermed.*, **2013**, *39*, 1655.
61. Jing, D.; Guo, L.; *J. Phys. Chem. Solids*, **2007**, *68*, 2363.
62. Maczka, M.; Knyazev, A.V.; Yu, K.N.; Ptak, M.; Macalik, L.; *J. Raman Spectrosc.*, **2011**, *42*, 529.
63. Liu, G.; Sun, C.; Yan, X.; Cheng, L.; Chen, Z.; Wang, X.; Wang, L.; Smith, S.C.; Lu, G.Q.; Cheng, H.M.; *J. Mater. Chem.*, **2009**, *19*, 2822.
64. Chen, S.; Yang, J.; Ding, C.; Li, R.; Jin, S.; Wang, D.; Han, H.; Zhang, F.; Li, C.; *J. Mater. Chem. A*, **2013**, *1*, 5651.
65. Venkataswamy, P.; Jampaiah, D.; Kandjani, A.E.; Sabri, Y.M.; Reddy, B.M.; Vithal, M.; *Res. Chem. Intermed.*, **2018**, *44*, 2523.
66. Kumar, V.N.; Priyanka, B.; Ravi, G.; Reddy, J.R.; Suresh, P.; Bhanuprakash, K.; Vithal, M.; *Eur. J. Inorg. Chem.*, **2014**, *2014*, 5585.
67. Varma, R.; Yadav, M.; Tiwari, K.; Makani, N.; Gupta, S.; Kothari, D.C.; Miotello, A.; Patel, N.; *Photochem. Photobiol.*, **2018**, *94*, 955.
68. Santos, D.M.D.; Navas, J.; Aguilar, T.; Sánchez-Coronilla, A.; Fernández-Lorenzo, C.; Alcántara, R.; Piñero, J.C.; Blanco, G.; Martín-Calleja, J.; *Beilstein J. Nanotechnol.*, **2015**, *6*, 605.
69. Reddy, J.R.; Sreenu, K.; Ravinder, G.; Suresh, P.; Kumar, V. N.; Ravi, G.; Vithal, M.; *Ceram Int.*, **2015**, *41*, 2869.
70. Panahi, P.N.; Rasoulifard, M.H.; Babaei, S.; *Rare Met.*, **2020**, *39*, 139.
71. Fang, Y.; Li, Z.; Yang, B.; Xu, S.; Hu, X.; Liu, Q.; Han, D.; Lu, D.; *J. Phys. Chem. C*, **2014**, *118*, 16113.
72. Nabih, S.; Shalan, A.E.; Serea, E.S.A.; Goda, M.A.; Sanad, M.F.; *J. Mater. Sci. Mater. Electron.*, **2019**, *30*, 9623.
73. Rawal, S.B.; Bera, S.; Lee, D.; Jang, D.J.; Lee, W.I.; *Catal. Sci. Technol.*, **2013**, *3*, 1822.
74. Ghayeb, Y.; Momeni, M.M.; Shafei, M.; *J. Iranian Chem. Soc.*, **2020**, *17*, 1131.
75. Sun, L.; Shao, Q.; Zhang, Y.; Jiang, H.; Ge, S.; Lou, S.; Lin, J.; Zhang, J.; Wu, S.; Donge, M.; Guo, Z.; *J. Colloid Interface Sci.*, **2020**, *565*, 142.
76. Liu, J.; Luo, Z.; Han, W.; Zhao, Y.; Li, P.; *Mater. Sci. Semicond. Process.*, **2020**, *106*, 104761.
77. Xia, Y.; He, Z.; Lu, Y.; Tang, B.; Sun, S.; Su, J.; Li, X.; *RSC Adv.*, **2018**, *8*, 5441.
78. Misra, M.; Chowdhury, S.R.; Singh, N.; *J. Alloys Compd.*, **2020**, *824*, 153861.

Authors biography

Sudheera Mannepalli did her M. Tech. in Chemical Engineering from Sri Venkateswara University, Tirupathi. Currently, she is working as Assistant Professor in Chemical Engineering Department at RVR & JC College of Engineering, Guntur, since 2012. At present, she is pursuing doctoral degree from Andhra University, Vishakhapatnam, India. Her Ph.D. topic is on "Photocatalytic studies of oxides for organic dye degradation".

Dr. Perala Venkataswamy obtained Ph.D. from Osmania University (2015). He is currently working as a SERB Research Associate in Osmania University. His research mainly focuses on developing novel heterogeneous catalysts for automotive exhaust purification and photocatalytic applications. He has authored about 35 peer-reviewed journals with an h-index of 13 and more than 755 citations. He has been received awards/fellowships, such as CSIR-JRF (2009) and Indo-Swiss Joint Research Program (2014), Dr. DS Kothari Postdoctoral Fellowship (2015).

Dr. Gundeboina Ravi received his M.Sc. Physical Chemistry from Kakatiya University, Warangal in 2009 and his Ph.D. in Chemistry from Osmania University in 2015 under the guidance of Prof. M. Vithal. Currently, he is working as Assistant Professor (part-time) of Chemistry in the University College of Science, Saifabad, Osmania University. He has 58 research publications in peer-reviewed journals. His research interests include synthesis of visible light active semiconducting materials for the energy and environmental applications.

Dr. Ramaswamy Kadari received his M.Sc. and Ph.D. Chemistry from Osmania University, Hyderabad. He is currently working as Technical Assistant at Centre for Materials for Electronics Technology (C-MET), Hyderabad. His research mainly focus on characterization of various samples, recovery of valuable metals from spent E-waste/LIBs/CFLs/PMs, synthesis, characterization and photoactivity of semiconducting materials for energy and environmental applications.

N. Chitti Babu did his Doctoral Degree in 2012 from Andhra University, Vishakhapatnam, India. Pursued his M.Tech in Environmental Engineering from Department of Chemical Engineering at IIT Madras, Chennai in 1997. He is working as Professor in Chemical Engineering Department at Andhra University, Vishakhapatnam, India since 2012. He has teaching experience of 22 years. Published 26 journals in Various National and International Journals. Around 14 Research papers presented in National/International Seminars, Conferences.

Dr. Muga Vithal obtained Ph.D. from the University of Hyderabad, Hyderabad and joined Osmania University as Assistant Professor in 1986. Presently, he is working as a BSR Faculty Fellow (UGC), India. His main areas of interest are solid state chemistry, structural identification, and the optical properties of solids as well as new materials, nanostructures and their photocatalyticproperties for energy and environmental applications.

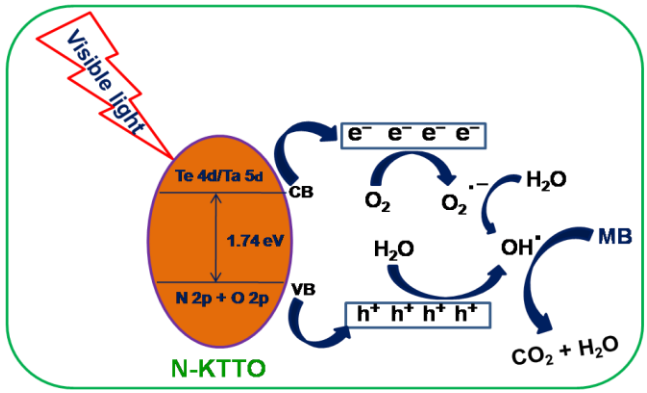

Scheme. 1. Schematic diagram of charge separation and photocatalytic degradation of the MB dye over N-KTTO under visible-light irradiation.

Graphical abstract

N-doped $KTaTeO_6$ showed the higher photoactivity towards the MB degradation owing to the higher surface area, narrow bandgap that leading to enhanced visible light absorption, reduced recombination of photogenerated electron-hole pairs and generation of larger amounts of hydroxyl radicals during the photocatalytic reaction, compared to parent KTTO.